

The Region of Large Sea Surface Height Variability in the Southeast Pacific Ocean

DAVID J. WEBB AND BEVERLY A. DE CUEVAS

Southampton Oceanography Centre, Southampton, United Kingdom

(Manuscript received 21 December 2001, in final form 30 October 2002)

ABSTRACT

Satellite altimeter observations of sea surface height (SSH) show an extensive triangular region of high variability in the southeastern Pacific. The region is unusual in two ways. First, it appears to have a horizontal correlation scale that is much larger than that associated with the mesoscale eddy-rich regions of the deep ocean. Second, the feature appears to reflect the shape of the underlying topography. Previous computer studies have suggested that it is a Rossby wave trapped by topography. Here detailed results are presented from a study that used a high-resolution global ocean model forced by 6-hourly ECMWF winds. The empirical orthogonal modes of the region are calculated, and it is shown that 29% of the SSH variance is due to a single mode with a similar shape to the region of high variability. The time series of the mode is correlated against the local Ekman pumping, and it is shown that the largest correlation is obtained when the lag is approximately 24 hours and the wind curl is averaged over a region roughly the size of the mode itself. The response function relating the amplitude of the mode time series to the amplitude of the forcing is calculated and is found to be dominated by a resonance at zero frequency and a decay time of 2.7 days. The results indicate that the feature is a highly damped geostrophic mode of the ocean.

1. Introduction

The study of sea level and its variability is one of the oldest branches of oceanography, but in recent years it has been enhanced by a wealth of new sea surface height (SSH) observations from satellite altimeters (Fu 2001). The observations have confirmed that in addition to shallow water regions where storm surges are an important factor, regions of high sea level variability are found near the equator, where equatorial Kelvin and Rossby waves are active, and at higher latitudes associated with boundary currents and mesoscale eddy activity. In the mesoscale eddy regions, the SSH variability has a complex horizontal structure with scales of order 100 km, similar to the scale of the underlying eddies.

In a few areas the satellite altimeter data also shows regions of enhanced SSH variability where the wavelengths appear much longer, typically 1000 km (Fu and Smith 1996; Fu 2001). One such region near 315°E, 45°S may be associated with the Zapiola eddy (Saunders and King 1995). Other regions are seen in the Pacific and Indian Oceans south of 45°S. In this paper we concentrate on the Southeast Pacific Basin where the long wavelength feature occupies a region bounded by the Antarctic continent, the Chile Rise, the East Pacific Rise, and its extension, the Pacific–Antarctic Rise.

This apparent trapping by the topography has been noted by previous authors. Thus Fu and Smith (1996) reported that the feature was primarily barotropic. Chao and Fu (1995) suggested that it was driven primarily by the curl of the wind field. Fukumori et al. (1998), using a low-resolution ocean model, found a spectral peak corresponding to a 28-day period, which they suggested may be due to topographically trapped Rossby waves (Willebrand et al. 1980; Leipold 1983). The model studies also show that much of the variability is at periods of less than a few days. Thus the signal is aliased in satellite-based observations of both SSH and gravity (Stammer et al. 2000; Tierney et al. 2000).

More recently Webb and de Cuevas (2002), working with results from a high-resolution baroclinic global ocean model, proposed that the feature was due to a zero frequency decaying mode of the ocean. Here we present a more detailed analysis of the model results and provide further evidence that the mode is not part of an oscillating system but that it is instead a zero frequency decaying mode.

The global ocean model used for the study is the 1/4° version of the Ocean Circulation and Climate Advanced Modelling Project (OCCAM) model (Webb et al. 1998a). When forced by 6-hourly winds from the European Centre for Medium-Range Weather Forecasts (ECMWF) reanalysis, the model reproduces both the mesoscale eddy field and long wavelength features seen in the satellite altimeter data. As previous authors (Ponte 1994; Gaspar and Ponte 1997) have found, the long wavelength fea-

Corresponding author address: Dr. David J. Webb, Southampton Oceanography Centre, Empress Dock, Southampton SO14 3ZH, United Kingdom.
E-mail: David.Webb@soc.soton.ac.uk

tures increase in amplitude slightly when surface pressure forcing is added to the model, but, if only monthly averaged winds are used, then they almost disappear.

To investigate the southeast Pacific feature in more detail, the empirical orthogonal functions are calculated for an area surrounding the region of high variability. This shows that the first mode, which explains 29.2% of the SSH variability, has a similar shape to the region of high variability. The second mode appears to be associated with wave motions around Antarctica.

The time series of the first mode is correlated with local Ekman pumping and the correlation is found to be largest when the pumping time series is lagged (delayed) 24 hours and averaged over a region of ocean roughly equal to the size of the mode. Assuming that the area average is a good approximation to the term forcing the mode, the response function relating this to the mode time series is calculated. The results are noisy but indicate that the mode is dominated by a single resonance at or near zero frequency. Analytic forms of the response function are fitted to the results, and give further support to the hypothesis that a zero-frequency damped mode is involved.

Section 2 of the paper describes the ocean model, the model runs used for the present investigation, and the SSH and bottom pressure variability seen in the different runs. Section 3 is concerned with calculating the empirical orthogonal modes of the SE Pacific, and section 4 with the correlation between the dominant mode and the Ekman pumping. Section 5 is concerned with the spectra of the two time series and this leads into section 6, which is concerned with the response function relating the Ekman pumping to the response of the ocean. Finally, section 7 is a discussion of the results.

2. The OCCAM model

OCCAM is a global primitive equation level model, based on the original Bryan–Cox–Semtner model (Bryan 1969; Semtner 1974; Cox 1984) but vectorized in the vertical. The model variables are potential temperature, salinity, the two horizontal components of velocity, and the sea surface height (above mean sea level). The model uses an Arakawa-B grid (Mesinger and Arakawa 1976) because of its superior performance in representing the propagation of short Rossby waves and fronts.

The model includes a number of developments of the basic Bryan–Cox–Semtner code to make it computationally efficient and to better represent ocean physics. The developments include replacing the rigid lid of the standard Bryan–Cox–Semtner model with a free surface. The resulting barotropic equations are solved using a simple tidal model (Webb et al. 1998a) with a time step of 18 s. Aliasing between barotropic waves with a period of one baroclinic time step and baroclinic waves with the same wavelength is prevented by stepping the tidal equations forward for two baroclinic time steps

and averaging the barotropic variables over this period. The baroclinic part of the model includes a surface layer of variable thickness, which enables a proper representation of rainfall and evaporation, improved advection schemes (Webb 1995; Webb et al. 1998b), and a double grid structure to allow improved representation of the Arctic Ocean. The internal organization of the code has also been changed so that it can run efficiently on modern high performance cache-based array processor computers using message passing (Webb 1996). Further details are given in Webb et al. (1998a).

The model uses Pakanowski and Philander (1981) vertical mixing for the tracer fields. For the velocity field, the model uses vertical Laplacian mixing with a coefficient of $1 \text{ cm}^2 \text{ s}^{-1}$. Laplacian mixing is also used to represent horizontal diffusion and viscosity with coefficients of $1 \times 10^6 \text{ cm}^2 \text{ s}^{-1}$ for diffusion and $2 \times 10^6 \text{ cm}^2 \text{ s}^{-1}$ for kinematic viscosity. Saunders et al. (1999) show that the model's SSH variability in the East Pacific is similar to that for the $\frac{1}{4}^\circ$ Parallel Ocean Program (POP) model (McCLean et al. 1997), which uses biharmonic friction.

The model topography was derived from the U.S. Navy $\frac{1}{12}^\circ$ DBDB5 dataset (U.S. Naval Oceanographic Office and U.S. Naval Ocean Research and Development Activity 1983) by calculating the median value for each model grid square and selecting the nearest model level. The depths of the key sills and channels were checked manually and adjusted where necessary (Thompson 1995). The potential temperature and salinity fields were initialized from the Levitus 1982 global annual average dataset (Levitus 1982). The velocity field was initially set to zero. Further details on the initial spinup phase of the model are given in Webb et al. (1998).

The initial run of the OCCAM model (denoted by WM) used smoothed monthly surface forcing fields. The surface wind stress was obtained by linearly interpolating, in space and time, the monthly climatology calculated by Barnier et al. (1995) from the ECMWF analysis during the period 1986–88. The surface heat flux was obtained by relaxing the surface layer to the Levitus and Boyer (1994) and Levitus et al. (1994) monthly values, using linear interpolation with a relaxation time of 30 days. The net effect of evaporation and precipitation was similarly represented by changing the sea surface height in such a way that, after conserving salinity, the salinity of the surface grid box converged on the Levitus value, again with a relaxation time of 30 days. Saunders et al. (1999) compare the model heat and freshwater fluxes in the Pacific with the National Centers for Environmental Prediction (NCEP)-STR climatology of Doney et al. (1998). In the South Pacific they find that the differences in the heat fluxes are about 10 W m^{-2} , comparable with the expected error of the observed flux. In contrast, they find that the model severely underestimates the net precipitation in the region. Such systematic errors will affect long-term trends in

the model but should not affect the main results and conclusions of the present paper.

The results presented here are primarily based on an additional run (denoted by W6) that starts from the beginning of year 8 of WM. In W6, the surface wind stress is linearly interpolated in space and time from the ECMWF 6-hourly analyses for the period 1992–93. In both these runs, WM and W6, the surface atmospheric pressure is assumed to be constant. This is normally justified on the basis that the ocean's response to surface pressure is primarily isostatic (Wunsch and Stammer 1997; Ponte 1994; Mathers and Woodworth 2001). As a check, in a third run (W6P), the model is also forced by varying sea surface pressure linearly interpolated from the ECMWF 6-hourly analyses.

Sea level and bottom pressure variability

As there have been relatively few runs of high-resolution global general circulation models, we briefly report here on the variability in the three OCCAM model runs. As in other high-resolution ocean models, the initial run of OCCAM produced an extensive mesoscale eddy field. This has a significant effect on the SSH field and, as seen in Fig. 1a, produces small-scale structures that dominate SSH variability in the Gulf Stream and Kuroshio Extension regions, in the Agulhas retroflection region, and along the path of the Antarctic Circumpolar Current. The model shows some variability at larger scales in the south Indian and Pacific Oceans but the model sea level variability at these scales is much less than that seen in the satellite data (Fu and Smith 1996).

When the monthly average wind forcing is replaced by 6-hourly forcing, two major changes occur (Fig. 1b). First, as seen in regions with very low variability, for example in the Pacific near Hawaii, there is an increase in the background rms SSH variability from less than 1 to more than 2 cm. Second, new structures are produced with a wavelength longer than those normally produced by the mesoscale eddy field. An example is the large triangular region in the SE Pacific. Near its center, at 48°S, 109°W the rms SSH variability is 1.9 cm with monthly winds increasing to 6.5 cm with 6-hourly winds. When 6-hourly surface pressure forcing is also added (Fig. 1c) the additional changes are much smaller. Thus at 48°S, 109°W the rms SSH variability is 6.9 cm, only just above the 6-hourly wind forced value.

The long wavelength features also affect the ocean bottom pressure variability (Fig. 2). In OCCAM the ocean bottom pressure P_z is defined as

$$P_z = g \int_z^\zeta \rho(z) dz + P_a, \quad (1)$$

where g is gravity, ρ is in situ density, ζ is sea surface height, z is depth (negative), and P_a sea surface pressure. For comparison with Fig. 1 pressure has been converted

to the equivalent SSH change, assuming that a SSH change of 1 cm produces a pressure change of 100.5 N m^{-2} ($1.005 \times 10^{-3} \text{ bar}$).

The results show that the bottom pressure variance is largest in the SE Pacific and Indian Ocean sectors of the Southern Ocean and that significant effects are also seen in the North Pacific, North Atlantic, and South Atlantic Oceans. In the SE Pacific, the rms bottom pressure at 48°S, 109°W is equivalent to an rms SSH of 1.9 cm when the model is forced by monthly winds (not shown). This increases to 5.8 cm when 6-hourly winds are used (Fig. 2) and to 6.6 cm with 6-hourly winds and pressure (not shown). In each case the background variability, that is, the typical minimum variability found in each ocean basin, is of order 1.5 cm.

As in other studies, we find that the fluctuations in the SE Pacific are primarily barotropic, in the 6-hourly wind run the rms difference between the surface and bottom pressure fluctuations being equivalent to less than 1.1 cm of water. Previous work (Ponte 1994) has shown that barotropic motions may be excited by Ekman pumping due to the wind or by changes in atmospheric pressure, but that Ekman pumping is usually most effective. The present results confirm this picture.

3. Empirical orthogonal modes

In the rest of this paper, we concentrate on the region of long wavelength variability in the SE Pacific. The SSH data is first processed to construct EOFs describing the variability. These are then used to investigate the connection with the surface forcing.

a. Method

Analysis was carried out using SSH data from the 2-yr run of the model forced by 6-hourly surface winds. The data covered a region of the South Pacific extending from 74.75° to 20.25°S and from 137.25° to 76.75°W. The full dataset comprises 2926 points in time and 52 756 points in space. For EOF analysis it is usual to remove the time mean at each point in the dataset. However, because precipitation and evaporation do not exactly cancel during the run, the small linear trend in SSH was also removed from the data.

Let $\eta(x_n, t_m)$ be the SSH at point x_n and time t_m after the mean and trend at each spatial point have been removed. The covariance matrix in space S and the total variance V are given by

$$S_{i,j} = \sum_m \eta(x_i, t_m) \eta(x_j, t_m), \quad (2)$$

$$V = \sum_n \sum_m \eta(x_n, t_m) \eta(x_n, t_m). \quad (3)$$

The EOFs are usually found by solving the eigenfunction equation

$$\sum_j (S_{i,j} - \lambda^k) e_j^k = 0, \quad (4)$$

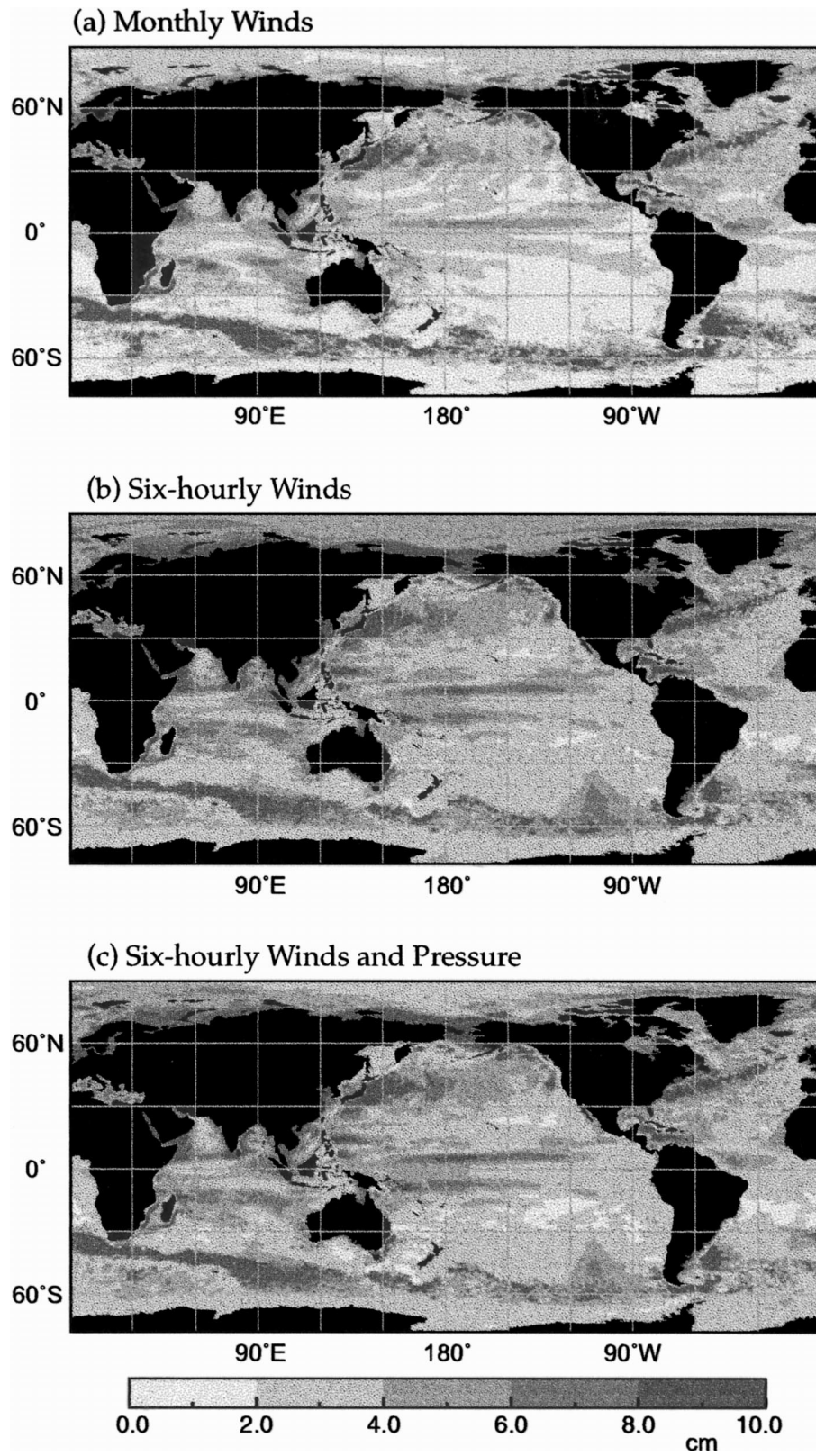


FIG. 1. The rms sea surface height of the OCCAM model when forced by linearly interpolated (a) monthly averaged winds, (b) 6-hourly winds, and (c) 6-hourly winds and pressure.

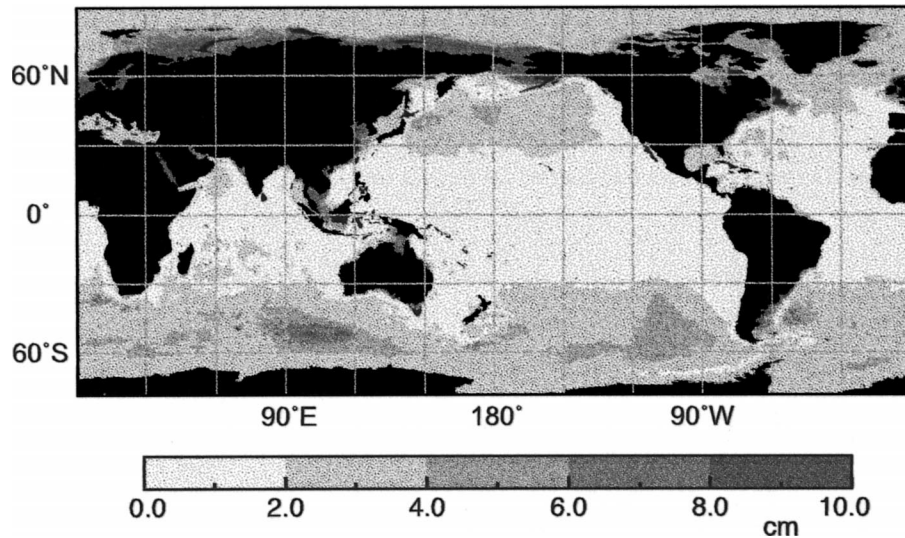


FIG. 2. The rms bottom pressure (expressed as the equivalent rms sea surface height) of the OCCAM model when forced by linearly interpolated 6-hourly winds (1 cm of seawater is equivalent to a pressure of 100.5 N m^{-2} or $1.005 \times 10^{-2} \text{ bar}$).

where the set of eigenvectors \mathbf{e} and eigenvalues λ are the required EOFs and their variances. However, as we have many more points in space than in time, it is computationally more efficient to work with the much smaller temporal covariance matrix S' :

$$S'_{ij} = \sum_n \eta(x_n, t_i) \eta(x_n, t_j). \quad (5)$$

The eigenvalue equation then becomes

$$\sum_j (S'_{ij} - \lambda^k) e_j^k = 0. \quad (6)$$

The nonzero eigenvalue solutions of this equation are the same as those of Eq. (4). The spatial EOFs (eigen-

vectors) \mathbf{e} are obtained from the time series (temporal eigenvectors) \mathbf{e}' using the relation

$$e^k(x_i) = \sum_j e'^k(t_j) \eta(x_i, t_j). \quad (7)$$

Scaled eigenvalues, which equal the fraction of the total variance V due to each of the EOFs, are given by

$$\Lambda^k = \lambda^k / V. \quad (8)$$

b. Results

The scaled eigenvalues Λ are plotted in descending order in Fig. 3 and the first four EOFs are shown in Fig. 4. The first EOF, which accounts for 29.2% of the total variance, is dominated by a central long wavelength feature (whose outline is given approximately by the 1.5 contour in Fig. 4a). The central region has roughly the same shape as the SE Pacific high variability region of Figs. 1b and 1c. However, in the south, along the path of the ACC, the mode also shows the effects of short wavelength noise due to mesoscale eddies.

The second EOF, which explains 9.5% of the variance, is dominated by mesoscale eddy activity and by sea level changes along the Antarctic coastline. Modes 3 and 4, explaining 8.1% and 7.0% of the variance, show evidence of standing oscillations within the region of high variability. Higher modes tend to be dominated by the mesoscale eddies but many also show longer wavelength features not necessarily restricted to the region of highest variability.

As a check that the results were robust, the analysis was repeated using a Gaussian horizontal filter to reduce the effect of mesoscale eddies and a cosine time filter to reduce end effects in the time series analysis. The

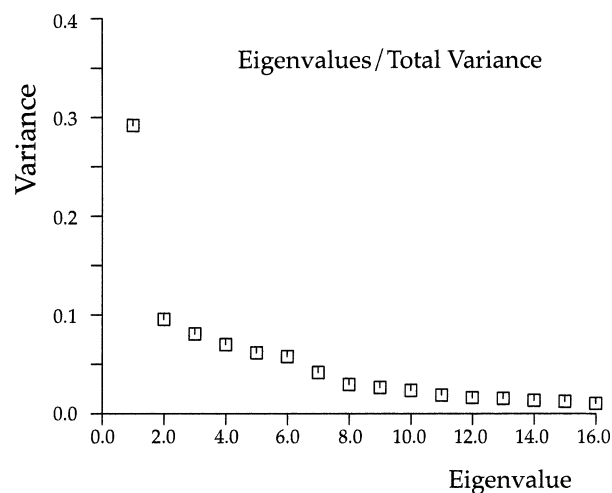


FIG. 3. The scaled eigenvalues [Eq. (7)] showing the fraction of the total SSH variance in the SE Pacific region explained by each of the empirical orthogonal modes.

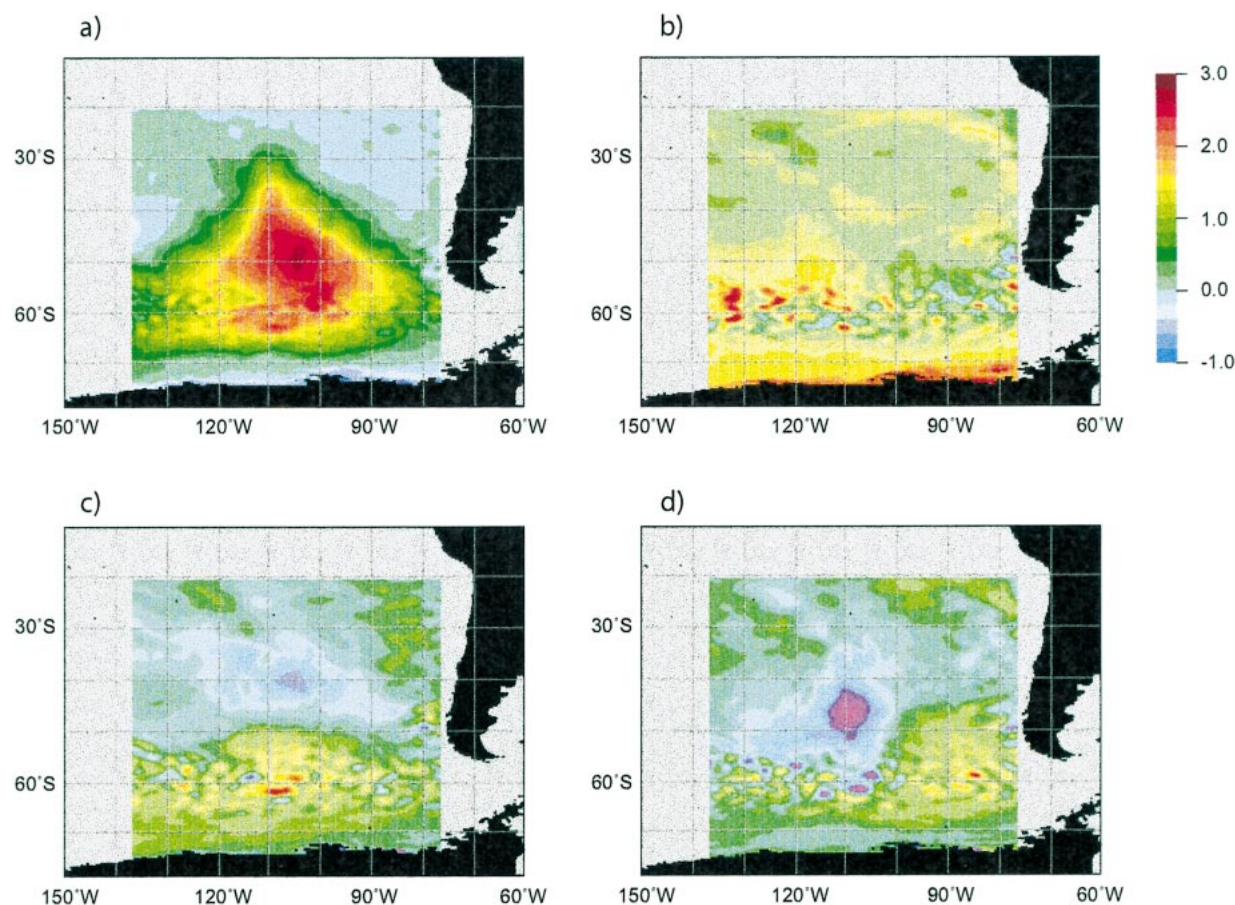


FIG. 4. The spatial structure of the first four empirical orthogonal modes, which explain (a) 29.2%, (b) 9.5%, (c) 8.1%, and (d) 7.0% of the total variance. The modes are normalized to have unit variance when averaged over the region shown. The modes are dimensionless, the corresponding time series [e' ; Eq. (7)] being defined to have a dimension of length.

Gaussian filter used a scale length of 139 km (1.25° north–south) in both directions. The results obtained doing this were essentially the same as before, the variance explained by the first four modes increasing to 32.8%, 12.8%, 9.2%, and 8.6%, respectively.

To investigate whether the modes are associated with progressive waves, the analysis was repeated using complex EOFs. Again the results were similar, the variance explained by the first four modes, being 29.7%, 14.9%, 10.2%, and 7.0%, respectively. More importantly, the spatial structures of the leading modes were also similar and there was no evidence of the phase shift found with progressive waves.¹

c. Spatial structure of the first EOF

In the rest of the paper we concentrate on the properties of the first EOF. If we ignore the effect of me-

oscale eddies in the solution, then the first EOF (Fig. 4a) is primarily confined to the SE Pacific basin, to a region bounded by the Antarctic continental shelf to the south and by the Chile Rise to the northeast. The crest of the Chile Rise is marked approximately by the 1.5 contour (Fig. 4a), the contour even following displacements in the ridge axis. To the northwest the EOF follows the line of the East Pacific Rise, but now the 1.5 contour runs along the western flank of the rise, indicating that the feature is not completely trapped by the topography.

This behavior is partly consistent with the mode being a barotropic mode controlled by contours of f/h (where h is depth and f is the Coriolis term). Plots of f/h (Koblinsky 1990), show that many of the contour lines from the SE Pacific basin cross to the western side of the midocean ridge near 30°S and continue southwest, eventually passing to the south of New Zealand. Thus this may be a route by which the mode loses energy. However, the mode (Fig. 4a) shows no evidence of the separate region of large f/h values that Koblinsky (1990) finds along the axis of the midocean ridge, for example near 50°S , 120°W .

¹ Further study indicates that there may be a progressive wave in a band near 1 rad day^{-1} coupling modes 3 and 4 of Fig. 4. However, its amplitude is too small for it to show as a separate complex empirical mode using the method described here.

4. Correlations

Figure 5 shows the rms amplitude of Ekman pumping and the correlation at zero lag between the Ekman pumping and the time rate of change of the first mode amplitude. The correlation $r(\tau)$ is defined as

$$r(\tau) = \frac{\sum_i p(t_i)q'(t_i + \tau)}{\left[\sum_j p(t_j)^2 \sum_k q'(t_k)^2 \right]^{1/2}}, \quad (9)$$

where t is time, p is the mean Ekman forcing, q' is the time rate of change of the first mode, and τ is the lag, positive when correlating the forcing with the time rate of change at a later time.

The calculations are based on the full set of 6-hourly data used for the EOF analysis. The Ekman pumping was calculated for the center points of each group of four wind stress points in the original ECMWF data file (in which the data point separation is approximately 1.125°).

The results show that, whereas the Ekman pumping only varies slowly with position, the correlation function has a very definite peak, the maximum value, 0.18, being found near 56°S , 113.5°W . This is slightly offset from the region where the mode itself has largest amplitude but the reason for the offset is not known.

The effect of changing the lag is shown in Fig. 6a. The solid line shows correlation between the Ekman pumping and the mode amplitude. It tends to zero at negative lags, as is required for causality, has a maximum at a lag of 36 h, and drops off relatively slowly for large positive lags. The correlation never becomes negative, as might be expected for correlations between a forcing function and a weakly damped oscillator.

The dashed line shows the correlation between the Ekman pumping and the rate of change of the first mode. The correlation again tends to zero at large negative lags, as is required for causality. It has a maximum at a lag of 6 h and becomes negative at large positive lags, implying that the mode is quickly damped.

a. The effect of scale

The shape of the high correlation region (Fig. 5b) suggests that the mode may be forced by the mean Ekman pumping acting over a similar large region of ocean. To investigate this idea further, the Ekman pumping was calculated for a series of regions of increasing size surrounding the initial point and the resulting time series correlated with the rate of change of the mode amplitude.

When this is done the largest correlations are obtained for the region bounded by 72° and 45°S and by 130° and 84°E (see Fig. 6b). The maximum correlation with the first mode time series is 0.74 and occurs at a lag of 24 h. The maximum correlation with the rate of change of the first mode is 0.48 and occurs at a lag of minus

12 h. As both correlations are significantly larger than those obtained at a single point, in the remainder of the paper we take the time series from this larger region to be our best estimate of the forcing field.

b. A simple model

One aspect of the above result, which caused concern, was the maximum correlation between the Ekman pumping and the rate of change of the first mode amplitude, found at a lag of minus 12 h. Because the maximum response of the ocean occurs before the forcing is a maximum, it may imply that the relationship is noncausal; that is, that Ekman pumping is not the forcing mechanism. However, the discrepancy (12 h) is less than the width of the autocorrelation function (the dotted line in Fig. 6b), so this may be a statistical effect.

To check if this is the case, we calculated the same lagged correlations for a simple model where we know causality must be satisfied. As before let the mode amplitude be $q(t)$ and the Ekman pumping $p(t)$. We have no information on how the mode decays, it may do so by radiating energy into other regions of ocean, but we will represent this decay by a term proportional to $q(t)$. The equation for the mode amplitude is then

$$\frac{\partial q}{\partial t} = p(t) - aq(t) + bn(t), \quad (10)$$

where a and b are unknown constants, $p(t)$ is the area averaged Ekman pumping used for Fig. 6b, and $n(t)$ is white noise of unit rms amplitude. The latter represents the random effect of the wind stress in other parts of the ocean. The constants a and b are chosen so that the lagged correlation between $p(t)$ and $q(t)$, where $q(t)$ is calculated from Eq. (10), is a best fit to the correlation curve of Fig. 6b. This gives values of a and b equal to 0.515 day^{-1} and 2.002 .

The resulting lagged correlation functions are shown in Fig. 6c. The correlation between $\partial q/\partial t$ and the Ekman pumping again shows the maximum correlation at a small negative lag. As Eq. (10) is strictly causal the result means that such a correlation pattern can occur without breaking causality. Also the calculated value of b corresponds to a decay time of 1.9 days, implying that the feature is rapidly damped.

5. Spectra

The autocorrelation functions indicate that at a single point (Fig. 6a) the Ekman pumping has a significant amount of energy at periods of less than a day. However, when it is averaged over a region of ocean (Fig. 6b), longer periods dominate. As the averaging also increases the correlation with the first mode, it is of interest to understand the changes in the spectrum in more detail. Here we do this by showing cumulative spectra, as these help to smooth out the noise in the spectral estimates.

At 56°S , 113.5°W where the single point correlation

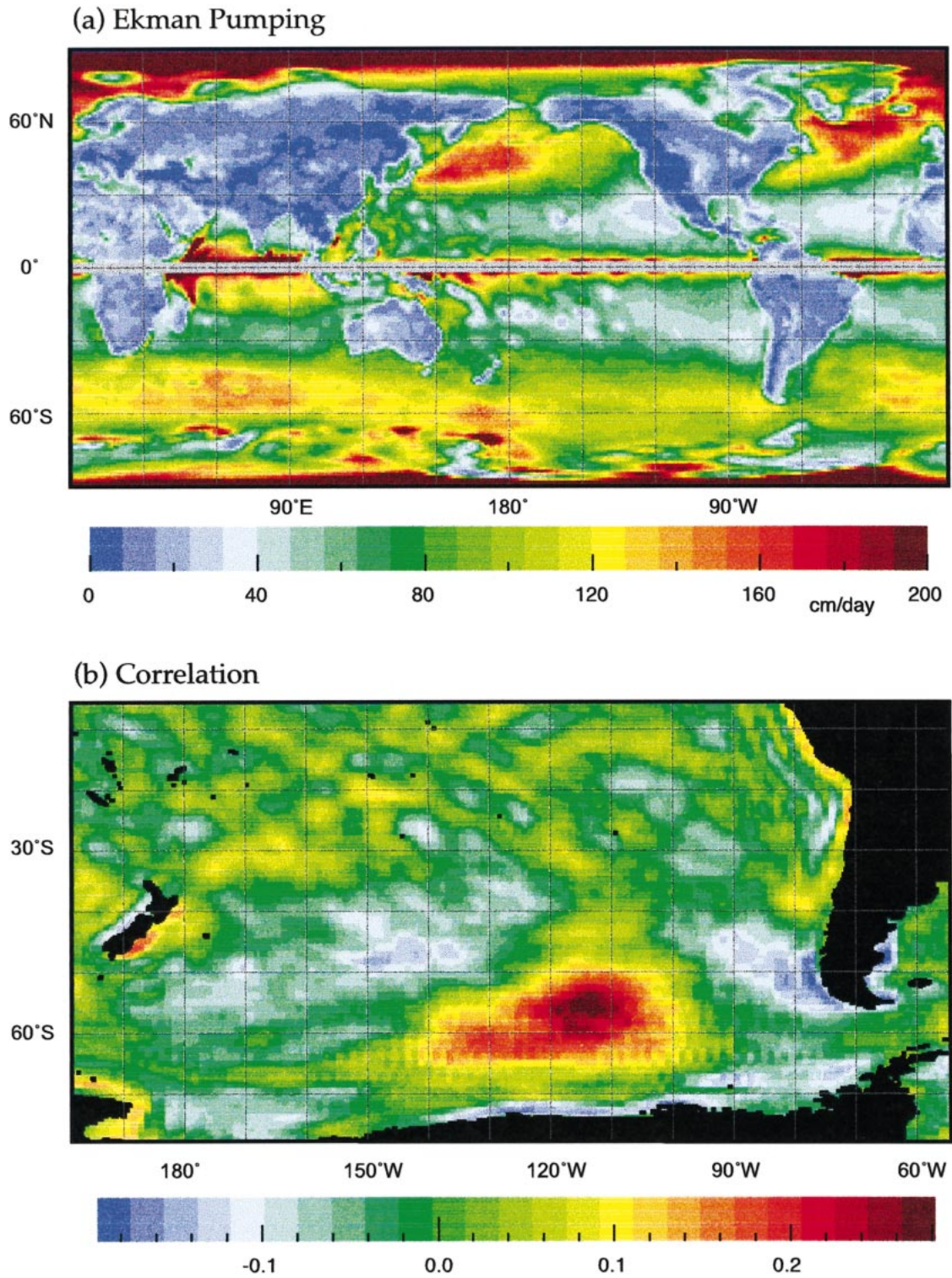


FIG. 5. (a) The rms amplitude of Ekman pumping (cm day^{-1}). (b) Correlation between the Ekman pumping at each point and the time series of the first mode.

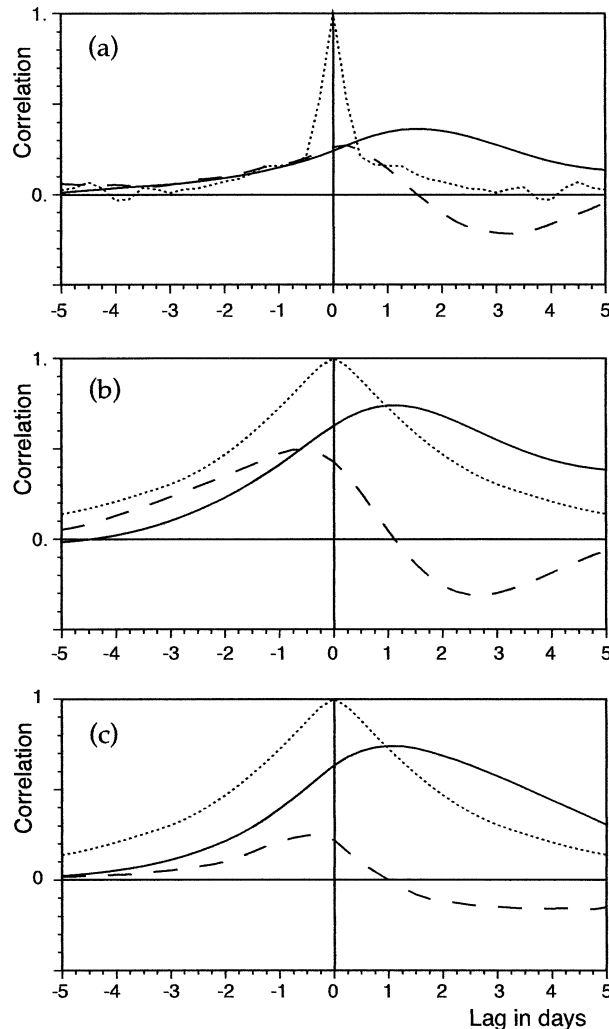


FIG. 6. (a) Correlation between the time series of Ekman pumping near 56°S, 113.5°W and the first-mode time series at different time lags. (b) Correlation between the Ekman pumping averaged over the region bounded by 72° and 45°S and by 130° and 84°E and the first mode. (c) Correlations for the simple model [Eq. (8)]. In each case the lines are solid: correlation with the mode amplitude, dashed: correlation with the mode time rate of change, and dotted: autocorrelation of the Ekman pumping time series.

is largest (Fig. 5b), the rms variance of the Ekman pumping is 68 cm day⁻¹. The cumulative spectrum (Fig. 7, line a) shows that about half the variance is at frequencies less than 1 rad day⁻¹ with most of the remainder in the band between 0.2 and 1 rad day⁻¹.

The area averaged Ekman pumping time series has a rms variance of 13.9 cm day⁻¹. The cumulative spectrum (Fig. 7, line b) confirms that the variance has moved to low frequencies, with over half at angular velocities below 0.4 rad day⁻¹ (i.e. periods of 16 days and longer). The first mode time series is also dominated by low frequencies with over half the amplitude variance at angular velocities below 0.1 rad day⁻¹ (Fig. 7, line c).

The vertical velocity spectrum can be obtained from

the amplitude spectrum by multiplying it by the square of the angular velocity. (The resulting spectrum corresponds to the vertical velocity at points in Fig. 4a at which the amplitude is 1.) The rms variance of the resulting vertical velocity is 0.21 cm day⁻¹. This is small compared with the 13.9 cm day⁻¹ Ekman pumping but as shown in Fig. 7 (line d) much more of the variance is now at 1 rad day⁻¹ and higher frequencies.

Overall these results imply that the mode amplitude is largest relative to the forcing at low frequencies but that the corresponding vertical velocities may be largest at high frequencies. To learn more we need to investigate the response function.

6. The response function

A classic method of investigating complex linear systems is to investigate the functional relationship between inputs or forces driving the system and the outputs or response of the system. Thus, Munk and Cartwright (1966) used the method to investigate the relationship between the tides at Honolulu and the tidal forcing. They proposed that the observed tide could be related to the equilibrium tide by the equation

$$q(t) = \sum_i w(\tau_i)p(t - \tau_i), \quad (11)$$

where $q(t)$ is the observed tide, $p(t)$ is the equilibrium tide, and their series of weights $w(\tau)$ represent the ocean's delayed response to an impulse at time zero. Because the system is causal, the weights should be zero when τ is less than zero.

The underlying physics of the system often becomes clearer in Fourier transform space. Let the real time series $p(t_j)$ consist of n samples at regular intervals ΔT and let $p(\omega_k)$ be the complex Fourier transform defined by

$$p(\omega_k) = \frac{1}{\sqrt{n}} \sum_{j=0}^{n-1} p(t_j) \exp\left(i \frac{2\pi j k}{n}\right), \quad (12)$$

where t_j equals $j\Delta T$ and ω_k equals $2\pi k/n\Delta T$. Let $q(\omega)$ be the corresponding Fourier transform of $q(t)$. The response function $R(\omega)$ is then defined as

$$R(\omega) = q(\omega)/p(\omega). \quad (13)$$

For linear systems, $R(\omega)$ is an analytic function with poles at the resonant frequencies of the system. If there is no friction in the system, the poles all lie on the real ω axis. If friction is present, the modes decay with time and the resonant poles move into the negative imaginary half plane. Causality also requires the poles to have negative imaginary components [see Webb (1973) for further details].

a. The southeast Pacific mode

We apply the approach to the present problem by assuming that the forcing term $p(t)$ is the Ekman forcing time series averaged as before over the region bounded

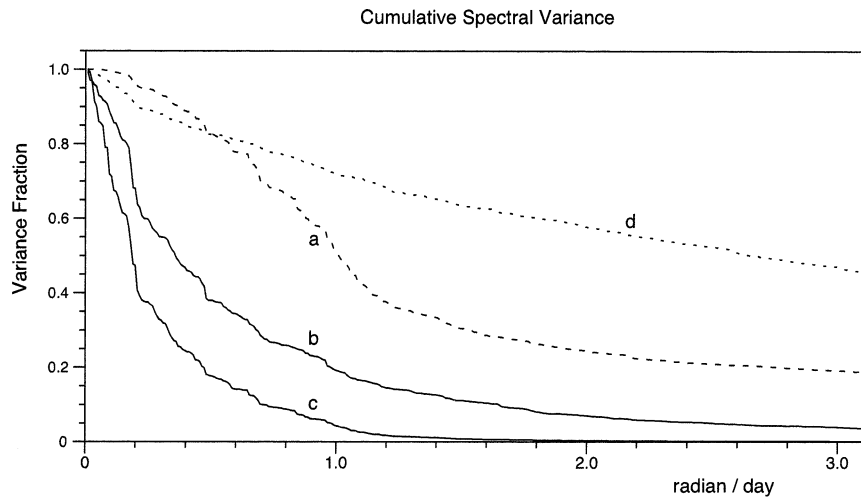


FIG. 7. Cumulative spectra (defined and normalized to have a value of one at the origin and zero at infinity) for (a) the Ekman pumping near 56°S , 113.5°W ; (b) the Ekman pumping averaged over the region bounded by 72° and 45°S and by 130° and 84°E ; (c) the first mode amplitude; and (d) the time rate of change of the first mode amplitude. The corresponding rms values of the un-normalized time series are (a) 68, (b) 13.9, (c) 2.8, and (d) 0.21 cm day^{-1} .

by 72° and 45°S and 130° and 84°E , and that the response $q(t)$ is the first mode time series. In reality, we expect $p(t)$ to be only a poor approximation to the true forcing, so the difference from the true forcing, the error term, may generate a considerable amount of noise in the results.

The response function relating $p(t)$ and $q(t)$ [Eq. (13)] is plotted in Fig. 8, the real and imaginary parts being plotted as functions of angular velocity. The raw data

points are very noisy but this can be reduced by averaging the data over groups of 21 adjacent frequencies.

These results show that the real part of the response function has a maximum at zero frequency, and the imaginary part has positive and negative peaks on either side of the origin. Such a pattern is characteristic of a single resonant pole and this conclusion is further confirmed when the averaged data is plotted on the complex plane as in Fig. 9. The data then show the classical

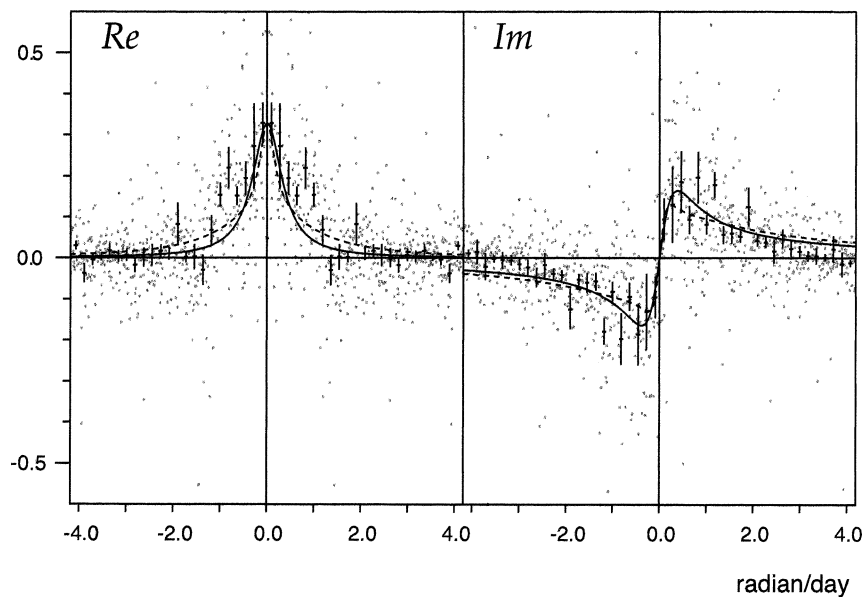


FIG. 8. Real and imaginary parts of the response function. Single dots correspond to individual samples, error bars to the mean and estimated error in the mean from averages over 21 adjacent samples. The solid (dotted) line is the best fit to the data using an analytic function with a single pole (two poles).

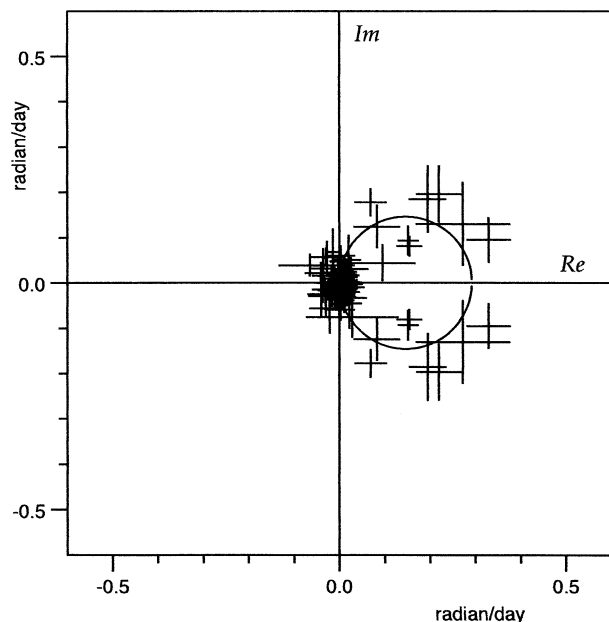


FIG. 9. Real and imaginary parts of the response function plotted on the complex plain. The error bars show the mean and estimated error in the mean obtained for averages over 21 adjacent samples. The solid line shows the best fit to the data obtained with an analytic function with a single pole.

circular structure associated with a single resonance (Webb 1982). The results imply that the response function is dominated by a single pole, which has zero real frequency and lies on the negative imaginary axis.

b. The decay time

The response function due to such a single resonance has the form

$$R(\omega) = A/(\omega - \omega_0), \quad (14)$$

where A is a constant and ω_0 the complex frequency corresponding to the resonant pole. One can show that for a general physical system with an unknown number of resonances, if $p(t)$ and $q(t)$ are real time series, then

$$\begin{aligned} p(\omega) &= p(-\omega^*)^*, & q(\omega) &= q(-\omega^*)^*, \\ R(\omega) &= R(-\omega^*)^*, \end{aligned} \quad (15)$$

where the asterisks represent complex conjugate. The last expression means that, if there is a pole at ω with residue R , then there is also one at $-\omega^*$ with residue $-R^*$. If the pole lies on the imaginary ω axis, as occurs with damped nonoscillating systems, then this condition is satisfied by a single pole with an imaginary residue.

Such a resonance arises when the time dependent behavior of the mode is described by a first-order equation; for example,

$$\frac{\partial q}{\partial t} = \gamma q = P \exp(-i\omega t), \quad (16)$$

where $q(t)$ is the amplitude of the mode, t is time, γ is the damping coefficient (also called the inverse decay time), and $P \exp(-i\omega t)$ is the forcing. The coordinate of the pole [ω_0 ; Eq. (15)] equals $-i\gamma$. The response of such a system is in phase with the forcing at very low frequencies and 90° out of phase at high frequencies.

If wave motions are involved then the equation describing the time dependent behavior is of second order,

$$\frac{\partial^2 q}{\partial t^2} + \gamma \frac{\partial q}{\partial t} + k^2 q = P \exp(-i\omega t). \quad (17)$$

The resulting response function is

$$\begin{aligned} R(\omega) &= A_+ / (\omega - \omega_+) - A_- / (\omega - \omega_-), \\ \omega_{+/-} &= -i(\gamma/2) \pm \sqrt{k^2 - (\gamma/2)^2}, \\ A_+ &= 1/(\omega_- - \omega_+), \quad A_- = -A_+. \end{aligned} \quad (18)$$

If friction is small, the two resonances lie symmetrically about the imaginary ω axis. If friction is large, then they both lie on the negative imaginary axis. In such oscillatory systems, the response is in phase with the forcing at low frequencies and out of phase at high frequencies.

Both forms of the response function were fitted to the data by minimizing the variance,

$$\sum_k |q(\omega_k) - r(\omega_k)p(\omega_k)|. \quad (19)$$

Because the true forcing function is unknown, the residues and the position of the resonances are both treated as unknowns, but ones that satisfy the symmetry relationships described above.

The best-fit single resonance, which explains 68% of the signal variance, is found when γ equals 0.37 day^{-1} (equivalent to a decay time of 2.7 days). This result, (see also Webb and de Cuevas 2002) is shown in Fig. 8 as a solid line. The agreement with the data is generally good, given that Eq. (19) weights frequencies where the spectrum is most energetic, that is, below 0.5 rad day^{-1} . However, there are some discrepancies between the analytic function and the data, indicating that additional resonances may be present, especially between 1.5 and 2.0 rad day^{-1} .

If the mode is part of an oscillating system, then it should be possible to obtain a better fit to the data using a response function with two poles. In a first test, the minimization is carried out assuming that the two residues are the negative of each other, as in Eq. (18). The resulting best fit, again explaining 68% of the variance, has one pole with the same position and residue as the single resonance solution. The second pole is at $-i7517 \text{ day}^{-1}$, a value that is probably physically unrealistic. The corresponding values of κ and γ [53 and 7517 day^{-1} ; Eq. (18)] are similarly unrealistically large.

In a second test, the only constraints on the solution are the symmetry constraints on the pole position and residues. The best-fit solution, which explains 70% of the variance, has poles at $-i0.2$ and $-i1.18 \text{ day}^{-1}$ (cor-

responding to decay times of 5.0 and 0.85 days, respectively). This result is the dotted line in Fig. 8. The improvement in the solution, over the single pole case, does not appear to be significant. However, both residues have the same sign as that of the single pole solution, so it is just possible that two (or more) damped modes are present.

7. Discussion

The good agreement between the model results and satellite observations in the SE Pacific indicate that the high-resolution ocean model has captured most of the physics responsible for the long wavelength SSH anomaly found in the region. Because of this we may have some confidence that the additional results obtained from the model have some relevance to the real ocean.

The model results confirm that the large wavelength feature is primarily barotropic and is driven by changes in the surface wind field. In addition, the analysis shows that the feature is due primarily to a single mode of the ocean and that it is forced by the mean Ekman pumping over an area roughly the size of the mode. The mode appears to be trapped by topography except for a region on the northwest side of the Pacific–Antarctic Rise. This could be a region where energy is being lost by the mode.

The changes in bottom pressure produced by the mode will affect the present generation of satellite-based gravity measurements. However, because there is only one dominant mode, it may be possible to correct for its effect using just the response function and a better estimate of the forcing function. Such an approach thus may be an alternative to the use of a full ocean model (Stammer et al. 2000) for correcting bottom pressure in such regions.

Although at present the forcing function is only known approximately, there is enough signal present to make an estimate of the response function. The result shows that the response function has its maximum amplitude at zero frequency and that it drops off at high frequencies with a limiting phase shift of 90° . Such behavior is consistent with a damped mode with zero real frequency.

This conclusion is further confirmed when analytic forms of the response function are fitted to the data. When a function with a single pole is used, a good fit is obtained when it has zero real frequency and a decay time of 2.7 days. When two poles are used, with residues related by the relationship typical of oscillating systems, then the best fit is obtained with one pole replicating the single pole solution and the second placed an unphysically large distance from the real axis. We conclude that it is unlikely that an oscillating mode is involved.

Instead the results suggest that the mode is behaving like a rapidly decaying Taylor column. If only bottom friction was involved, then the spindown time would be very long. However, the present mode may be losing

energy rapidly along the Pacific–Antarctic Rise. Further studies will be needed to see if this is indeed the case.

Acknowledgments. We acknowledge the contributions of Dr. A. Coward, Dr. C. Richmond, and Miss E. Rourke in developing and running the OCCAM ocean model. Thanks also are given for the comments of the anonymous referees.

REFERENCES

- Barnier, B., L. Siefridt, and P. Marchesio, 1995: Thermal forcing for a global ocean circulation model using a three-year climatology of ECMWF analyses. *J. Mar. Syst.*, **6**, 363–380.
- Bryan, K., 1969: A numerical method for the study of the circulation of the world ocean. *J. Comput. Phys.*, **4**, 347–376.
- Chao, Y., and L.-L. Fu, 1995: A comparison between the TOPEX/POSEIDON data and a global ocean general circulation model during 1992–1993. *J. Geophys. Res.*, **100**, 24 965–24 976.
- Cox, M. D., 1984: A primitive equation 3-dimensional model of the ocean. GFDL Ocean Group Tech. Rep. No. 1, 143 pp. [Available from Geophysical Fluid Dynamics Laboratory/NOAA, Princeton University, Princeton, NJ 08542.]
- Doney, S. C., W. G. Large, and F. O. Bryan, 1998: Surface ocean fluxes and water-mass transformation rates in the coupled NCAR Climate Model. *J. Climate*, **11**, 1420–1441.
- Fu, L.-L., 2001: Ocean circulation and variability from satellite altimetry. *Ocean Circulation and Climate*, G. Siedler et al., Eds., Academic Press, 141–172.
- , and R. D. Smith, 1996: Global ocean circulation from satellite altimetry and high-resolution computer simulation. *Bull. Amer. Meteor. Soc.*, **77**, 2625–2636.
- Fukumori, I., R. Raghunath, and L.-L. Fu, 1998: The nature of global large-scale sea level variability in relation to atmospheric forcing: A modeling study. *J. Geophys. Res.*, **103**, 5493–5512.
- Gaspar, P., and R. M. Ponte, 1997: Relation between sea level and barometric pressure determined from altimeter data and model simulations. *J. Geophys. Res.*, **102**, 961–971.
- Koblinsky, C. J., 1990: The global distribution of f/H and the barotropic response of the ocean. *J. Geophys. Res.*, **95**, 3213–3218.
- Leipold, G., 1983: Vorticity oscillations over closed f/h contours. Hamburger Geophysikalische Einzelschriften, Rep. 60, Geophysical Institute of the University of Hamburg, 94 pp.
- Levitus, S., 1982: *Climatological Atlas of the World Ocean*. NOAA Prof. Paper 13, 173 pp. and 17 microfiche.
- , and T. P. Boyer, 1994: *Temperature*. Vol. 4, *World Ocean Atlas 1994*, NOAA Atlas NESDIS 4, 117 pp.
- , R. Burgett, and T. P. Boyer, 1994: *Salinity*. Vol. 3, *World Ocean Atlas 1994*, NOAA Atlas NESDIS 3, 99 pp.
- Mathers, E. L., and P. L. Woodworth, 2001: Departures from the local inverse barometer model observed in altimeter and tide gauge data and in a global barotropic numerical model. *J. Geophys. Res.*, **106**, 6957–6972.
- McClean, J. L., A. J. Semtner, and V. Zlotnicki, 1997: Comparisons of mesoscale variability in the Semtner-Chervin $1/4^\circ$ model, the Los Alamos Parallel Ocean program $1/6^\circ$ model and TOPEX/POSEIDON data. *J. Geophys. Res.*, **102**, 25 203–25 226.
- Mesinger, F., and A. Arakawa, 1976: *Numerical Methods Used in Atmospheric Models*. GARP Publication Series No. 17, World Meteorological Organization, Geneva, 64 pp.
- Munk, W. H., and D. E. Cartwright, 1966: Tidal spectroscopy and prediction. *Philos. Trans. Roy. Soc. London*, **259A**, 533–581.
- Pacanowski, R. C., and S. G. H. Philander, 1981: Parameterization of vertical mixing in numerical models of tropical oceans. *J. Phys. Oceanogr.*, **11**, 1443–1451.
- Ponte, R. M., 1994: Understanding the relation between the wind and pressure-driven sea level variability. *J. Geophys. Res.*, **99**, 8033–8039.

- Saunders, P. M., and B. A. King, 1995: Bottom currents derived from a shipborne ADCP on WOCE cruise A11 in the South Atlantic. *J. Phys. Oceanogr.*, **25**, 329–347.
- , A. C. Coward, and B. A. de Cuevas, 1999: The circulation of the Pacific Ocean seen in a Global Ocean Model (OCCAM). *J. Geophys. Res.*, **104**, 18 281–18 299.
- Semtner, A. J., 1974: A general circulation model for the World Ocean. Department of Meteorology Tech. Rep. 9, University of California, Los Angeles, 99 pp.
- Stammer, D., C. Wunsch, and R. M. Ponte, 2000: De-aliasing of global high frequency barotropic motions in altimeter observations. *Geophys. Res. Lett.*, **27**, 1175–1178.
- Thompson, S. R., 1995: Sills of the global ocean: A compilation. *Ocean Modelling*, **109** (unpublished manuscripts), 7–9.
- Tierney, C., J. Wahr, F. Bryan, and V. Zlotnicki, 2000: Short period oceanic circulation: Implications for satellite altimetry. *Geophys. Res. Lett.*, **27**, 1255–1258.
- U.S. Naval Oceanographic Office and U.S. Naval Ocean Research and Development Activity, 1983: DBDB5 (Digital Bathymetric Data Base) 5 minute grid. Bay St. Louis, MS.
- Webb, D. J., 1973: Green's function and tidal prediction. *Rev. Geophys. Space Phys.*, **12**, 103–116.
- , 1982: Tides and tidal energy. *Contemporary Phys.*, **23** (5), 419–442.
- , 1995: The vertical advection of momentum in Bryan–Cox–Semtner ocean general circulation models. *J. Phys. Oceanogr.*, **25**, 3186–3195.
- , 1996: An ocean model for array processor computers. *Comput. Geosci.*, **22** (5), 569–578.
- , and B. A. de Cuevas, 2002: An ocean resonance in the Southeast Pacific. *Geophys. Res. Lett.*, **29**, 93-1–93-3.
- , —, and A. C. Coward, 1998a: The first main run of the OCCAM global ocean model. Southampton Oceanography Centre Internal Rep. 34, 44 pp.
- , —, and C. S. Richmond, 1998b: Improved advection schemes for ocean models. *J. Atmos. Oceanic Technol.*, **15**, 1171–1187.
- Willebrand, J., S. G. H. Philander, and R. C. Pacanowski, 1980: The oceanic response to large scale atmospheric disturbances. *J. Phys. Oceanogr.*, **10**, 411–429.
- Wunsch, C., and D. Stammer, 1997: Atmospheric loading and the oceanic “inverted barometer” effect. *Rev. Geophys.*, **35**, 79–107.